Catalysis Today 433 (2024) 114658

Contents lists available at ScienceDirect

Catalysis Today

journal homepage: www.elsevier.com/locate/cattod

Effect of Nb as dopant of hydrotalcite catalysts during the ethanol condensation to optimize *n*-Butanol production

Daniel Alejandro Valdivieso-Vera [a,b], Gerardo Antonio Flores-Escamilla [a], José Julián Cano-Gómez [a], Isabel Barroso-Martín [c], Enrique Rodríguez-Castellón [c], Iván Alonso Santos-López [a,*], M. Olga Guerrero-Pérez [b,*]

[a] Facultad de Ciencias Químicas, Universidad Autónoma de Nuevo León, San Nicolás de los Garza, Nuevo León 66455, Mexico
[b] Departamento de Ingeniería Química, Universidad de Málaga, Campus Teatinos, Málaga 29071, Spain
[c] Departamento de Química Inorgánica, Cristalografía y Mineralogía, Facultad de Ciencias, Universidad de Málaga, Campus Teatinos, Málaga 29071, Spain

ARTICLE INFO

Keywords:
Bioethanol
n-Butanol
Copper
Niobium
Hydrotalcite
Guerbet reaction

ABSTRACT

The present study optimizes Cu-supported catalysts on hydrotalcite for the synthesis of *n*-butanol whose interest is in its use as biofuel, due to its superior performance in comparison with other short-chain alcohols. The catalytic performance was improved by adding Nb to the catalytic formulation. In this way, several Cu-Nb catalysts supported on hydrotalcites (Mg/Al) with different Nb loadings were synthesized by incipient wetness impregnation and characterized by H_2−temperature-programmed reduction, X-ray diffraction, N_2 physisorption, CO_2− and NH_3−thermo-programmed desorption and X-ray photoelectron spectroscopy. It was shown that the incorporation of Nb promoted a suitable balance between the acid-basic and redox sites, modulating the Cu^0/Cu^+ dehydrogenation/hydrogenation properties for the *n*-BuOH production. The synthesis of multiple value-added products (*n*-BuOH, acetaldehyde, ethyl acetate, and 1-hexanol) was achieved in both the liquid− (at 180 °C) and gas−phase (150−350 °C), where it was demonstrated that both the *n*-BuOH selectivity and ethanol conversion improved with the Nb addition. The performance of the catalysts under time on stream and their recycling ~~is~~ also described.

1. Introduction

Higher alcohols, including *n*-Butanol (*n*-BuOH), have emerged as a promising biofuel, as they are demonstrated to be crucial for several applications in the renewable energy landscape [1–3]. They have many advantages, including a high energy content, low water solubility, and they are compatible with existing infrastructure and engines [4]. In contrast to ethanol (EtOH), which is the most produced biofuel globally, *n*-butanol is not miscible in water, avoiding separation and corrosion problems in engines [5]. Also, *n*-butanol can be blended with gasoline at higher ratios than ethanol [6].

n-BuOH can be produced from biomass feedstocks by fermentation [2,7–10]. Furthermore, as a biochemical method, it has some limitations that a heterogeneous catalytic method would overcome. In this sense, the Guerbet coupling reaction is quite promising. It is a condensation that involves several steps: 1) dehydrogenation of the starting alcohols to give the corresponding aldehydes; 2) aldol condensation of the aldehydes; 3) dehydration; and 4) hydrogenations of the unsaturated aldol condensation products to give higher Guerbet alcohols [11,12].

Metal oxide-based catalysts, such as MgO, are promising catalysts for the Guerbet reaction. Birky et al. reported that the EtOH self-condensation over MgO produces *n*-BuOH and acetaldehyde (ACe), and ethene as byproducts in a fixed-bed reactor at 400 °C [13]. γ -Al_2O_3 provides high EtOH conversion and diethyl ether and ethylene as main products at 300 °C [14]. The distribution of products is closely tied to the distribution of acid and basic sites. Hydrotalcite (HT)-derived mixed oxides (Mg/Al) have also been tested for the EtOH coupling to *n*-BuOH [15]. A high hydrogenation capacity is observed when the number of Mg species in HT increases [16]. The addition of Cu to HT improves the EtOH dehydrogenating activity and modifies the product distribution [17–20]. Benito et al. reported CuMgAl catalysts for the EtOH condensation in the liquid phase at 200 °C and obtained mainly two higher alcohols: *n*-BuOH and 1-hexanol (1-HexOH). Additionally, they produce ethyl acetate (AcOEt) [17]. The selectivity towards AcOEt is mainly

* Corresponding authors.
E-mail addresses: ivan.santoslp@uanl.edu.mx (I.A. Santos-López), oguerrero@uma.es (M.O. Guerrero-Pérez).

https://doi.org/10.1016/j.cattod.2024.114658
Received 20 January 2024; Received in revised form 15 March 2024; Accepted 18 March 2024
Available online 19 March 2024

related to the acidity of the catalyst [19]. On the other hand, catalysts with acid sites are more selective to *n*-BuOH than catalysts considered "fully basic" [21–24]. Tsuchida et al. studied the synthesis of *n*-BuOH over hydroxyapatite materials [23]. They reported that an increase in the surface acidity of the catalysts might indicate an improvement in selectivity towards *n*-BuOH. Thus, to improve the catalytic formulation it is necessary to modulate the acidity and also the redox sites, and this can be achieved by using a dopant such as Nb. Niobium is able to modulate catalytic redox properties and increase the number of acid sites, and its ability to promote catalyst performance by promoting the entanglement of other elements in mixed oxide catalysts has been demonstrated with many catalytic formulations [25–33]. In addition, some reaction products and byproducts, such as ACe resulting from the dehydrogenation of EtOH [20], can be oxidized in the presence of niobium-containing catalysts to form acetic acid, which subsequently couples to another molecule of EtOH to produce AcOEt due to its redox properties and increased acidity [28,29], which is a valuable byproduct.

The main objective of the present work is to improve the catalytic properties during the ethanol condensation of Cu/HT catalysts using Nb as a dopant. To this end we have prepared and characterized several Cu_{10}-Nb_x/HT catalysts with different Nb loadings to correlate the catalytic activity performances with their main chemical structure, to optimize the *n*-BuOH synthesis.

2. Materials and methods

2.1. Catalysts synthesis

The mixture of oxides of $Mg_xAl_yO_z$ (HT 3) from the thermal decomposition of hydrotalcite Mg/Al molar ratio of 3 used as support was synthesized by the co-precipitation method [34]. In a typical synthesis, magnesium nitrate hexahydrate ($Mg(NO_3)_2 \cdot 6H_2O$, Sigma Aldrich) and aluminum nitrate nonahydrate ($Al(NO_3)_3 \cdot 9H_2O$, Sigma Aldrich) were simultaneously added to dropwise into a beaker. Then, 25 mL of 1 M sodium carbonate (Na_2CO_3, Sigma Aldrich) were added drop by drop. The resulting suspension was first sonicated for 20 min and then stirred and adjusted with 2 M hydroxide sodium (NaOH, Sigma Aldrich) solution to a pH of 9−10. The solution was kept under magnetic agitation for 1 h. Subsequently, the precipitate was washed several times with hot distilled water, and it was recovered by filtration and dried at 60 ºC overnight. Finally, the hydrotalcite powder was calcined at 500 ºC for 2 h to obtain mixed oxides support with a 3 Mg/Al molar ratio, namely HT 3.

Niobium was supported by incipient wetness impregnation, using niobium (V) oxalate hydrate/oxalic acid solutions with values of Nb of 0.5, 2.5 and 5 wt%. The solids were dried at 60 ºC overnight and then calcined at 500 ºC for 4 h. Then, 10 wt% Cu ($Cu(NO_3)_2 \cdot 3H_2O$, Sigma Aldrich) was incorporated into all catalysts by incipient wetness impregnation. The final catalysts were dried at 60 ºC overnight, calcined in static air at 500 ºC for 2 h, and finally reduced at 400 ºC for 4 h in a 30 mL/min H_2 flow. The catalysts have been identified as Cu_{10}-Nb_x/HT 3, where "x" is 0.5, 2.5, or 5 Nb wt%.

2.2. Catalyst characterization

Powder diffraction patterns were collected on a Bruker D8 ADVANCE diffractometer using MoKα_1 radiation. The detection system consists of an EIGER detector (from DECTRIS) specially designed and optimized for Mo anodes, the detector was used with an aperture of 4 ×21 degrees, working in VDO mode. Crystalline structures were obtained within Bragg 2θ angle from 2.5 to 45° during 120 min. The tube worked at 40 kV and 45 mA.

N_2 adsorption-desorption isotherms at −196 °C were performed with an ASAP 2020 (Micromeritics). Prior to N_2 adsorption, all samples were degasified at 200 °C. Temperature-programmed H_2 reduction was carried out in an AutoChem III system (Micromeritics). For 30 min, the catalyst was cleaned at 150 ºC with a 50 mL/min He flow. The carrier gas was changed to 5% H_2/Ar (v/v) at 30 mL/min after cooling to 50 ºC. When the baseline was stable, the temperature was raised to 800 ºC at a rate of 10 ºC/min, while the amount of H_2 consumed was measured using GC-TCD. The samples were calcined and reduced *in-situ* as was mentioned in Section 2.1.

Temperature-programmed NH_3 and CO_2 desorption tests were carried out in Autochem III (Micromeritics) equipment using powdered catalysts. Samples were pretreated in a quartz tubular reactor at 500 ºC at a rate of 30 mL/min He flowed for 2 h. Before the adsorption of NH_3 and CO_2, the samples were reduced *in situ* at 400 ºC at a rate of 30 mL/min H_2 flowed for 2 h, then was cooled to 40 ºC and subjected for 15 mi to a 10% NH_3/He (v/v) or 10% CO_2/He (v/v) stream at a flow rate of 30 mL/min. He purged (30 mL/min) for 30 min and removed the physisorbed NH_3 and CO_2. Subsequently, the samples were heated at a ramp rate of 10ºC/min up to 800 ºC and the desorbed NH_3 or CO_2 was monitored and recorded using a GC-TCD and GC-MS. The equipment was previously calibrated with 10% NH_3/He and CO_2.

X-ray photoelectron spectroscopy (XPS) data were acquired using a Physical Electronics PHI 5700 spectrometer with non-monochromatic Mg-K radiation (300 W, 15 kV, 1253.6 eV) and a multichannel detector for the examination of the core level signals of the examined elements. Spectra of powdered samples were acquired utilizing a 720 μm diameter analysis area and a constant pass energy value of 29.35 eV. All the samples were calcined and reduced *ex-situ* before the analysis as mentioned in Section 2.1, unless otherwise specified.

2.3. Catalytic tests

2.3.1. Catalytic activity for the ethanol condensation in a Batch reactor

The ethanol condensation was performed in a batch system in a stainless-steel reactor with 100 mL of ethanol and 200 mg (0.106−0.125 mm) of previously activated powdered catalyst (Section 2.1). The reaction was carried out at 180 °C with stirring at 800 rpm and under 30 atm of N_2 pressure. Following the reaction profile, samples were collected at different times through the sample valve and quickly cooled at 0 ºC. Every hour for 6 h, reaction samples were collected, dissolved with 1-pentanol and 1–3-dichlorobenzene as internal standards, and stored in sealed vials for gas chromatography analysis using a Shimadzu GB-14A chromatograph equipped with a flame ionization detector and a CP-Wax 52 CB capillary column.

2.3.2. Catalytic activity for the ethanol condensation in a continuous flow reactor

Ethanol condensation was carried out in a tubular metal flow reactor with an internal diameter of 9.1 mm. 200 mg of pelletized catalyst (0.71−0.85 mm) was inserted into the reactor and diluted with silicon carbide (SiC, VWR Chemicals) up to 3 mL for these reaction studies. The catalysts were reduced *in situ* for 2 h at 400 ºC using a 50 mL/min H_2 flow and a 5 ºC/min heating rate. The reactions were carried out at 150, 200, 250, 300, and 350 ºC at atmospheric pressure with a liquid feed flow of 0.1 mL/min and a N_2 flow of 30 mL/min after cooling to 150 ºC. These conditions were optimized to avoid internal and external diffusional limitations. After recovering the catalyst, drying it at 60 ºC overnight, and characterizing it by N_2 physisorption and XPS, reusability investigations were carried out at the optimum reaction temperature. The reaction samples were analyzed as mentioned in Section 2.3.1.

3. Results and discussion

3.1. Characterization of Cu_{10}-Nb_x/HT 3 catalysts

The Cu_{10}-Nb_x/HT 3 catalysts showed the typical diffraction patterns of the MgO periclase structure at 2θ = 17, 27 and 34º according to JCPDS 01-085-5620 (Fig. 1) [34,35]. The niobium oxide pattern was detected at 16º (JCPDS 00-047-1694) and its intensity increases when Nb

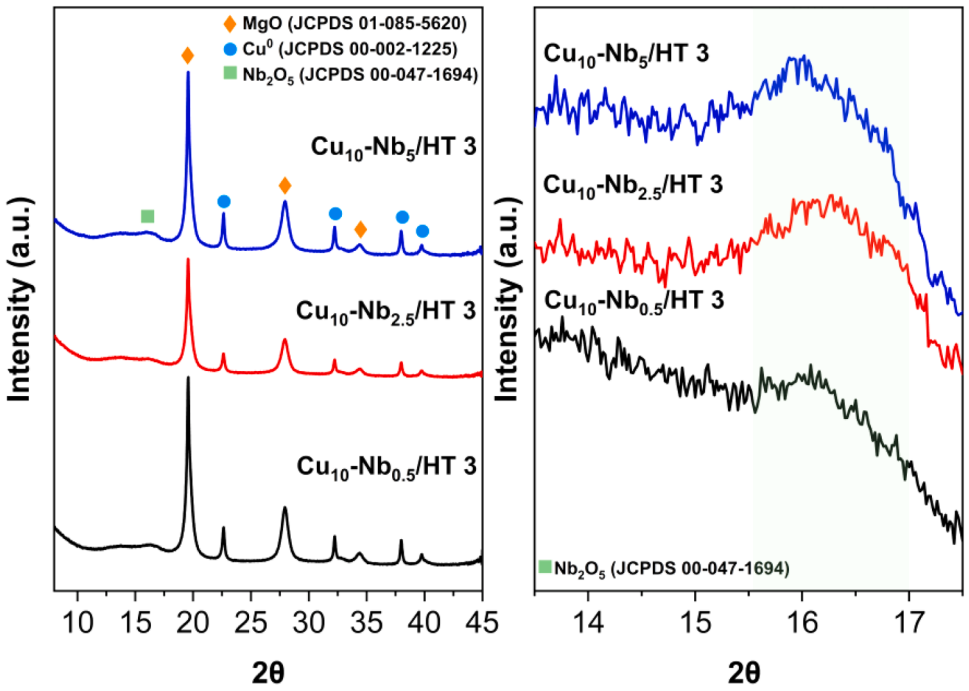

Fig. 1. Powder X-ray diffraction patterns of Cu_{10}-Nb_x/HT 3 calcined at 400 °C for 2 h in static air and ex-situ reduced with H_2 at 400 °C for 2 h: as a function of Nb wt%.

loadings increase from 0.5 to 5 wt% [36,37]. The crystallite size of Nb_2O_5 calculated with Scherrer equation varies from 4.0 to 4.8 nm, as a function of the Nb wt%. Additionally, Cu^0 crystalline phase was detected at 2θ = 23, 32, 36 and 39° (JCPDS 00-002-1225) [38]. The crystallite sizes of Cu^0 were in the 16.2–17.4 nm range. These data show that there was an increase in the Cu crystallite size when adding Nb, since the Cu_{10}/HT 3 catalyst (in the absence of Nb) presented a crystallite size of 10.4 nm. This indicates that the incorporation of Nb into the catalyst promoted the growth of Cu crystallites.

The H_2–TPR profiles of Cu_{10}-Nb_x/HT 3 are shown in Fig. 2. A broad reduction peak was primarily attributed to the reduction of highly dispersed Cu^{2+} species to Cu^+ and finally to Cu^0 at ≈400 °C [38,39]. This was confirmed with the XRD data, which revealed that Cu^0 was detected in the Cu_{10}-Nb_x/HT 3 catalysts after their reduction for 2 h at 400 °C in an H_2 atmosphere. The reduction of Nb_2O_5 to NbO_2 has been reported to occur mainly at higher temperatures, as a result, no reduction event was found at the temperatures depicted in the reduction profiles. [36].

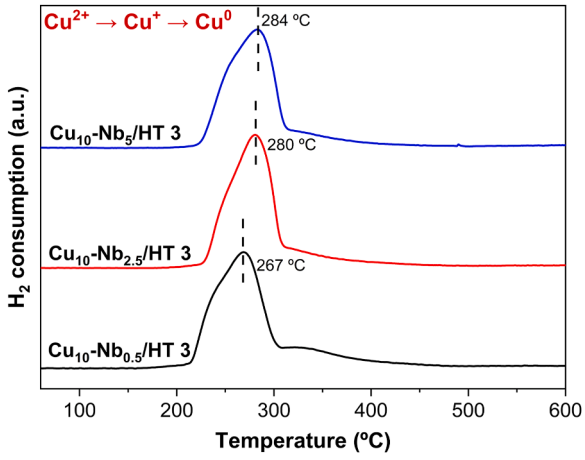

Fig. 2. H_2–TPR profiles for the Cu_{10}-Nb_x/HT 3 calcined at 400 °C for 2 h in static air: as a function of Nb wt%.

However, the catalyst reduction process was carried out at 400 °C, therefore NbO_2 was not expected to be found in the catalyst. The XRD results showed that the only crystalline phase present is Nb_2O_5, and that the NbO_2 species may not be present in the catalyst or may be in low proportions for the Nb_2O_5 species. This assumption was confirmed by XPS and will be discussed later. A slight increase in the temperature of the reduction peak was observed with increasing the Nb loading on the catalyst, indicating some Nb–Cu interactions. The reduction profile of the Nb-free catalyst is in Supplementary Information (Figure S1).

The N_2 isotherms correspond to Type IV (Figure S2) according to the IUPAC classification [40], confirming the mesoporous nature of the Cu_{10}-Nb_x/HT 3 catalysts. The BET-specific surface area (SSA) and average pore diameter of Cu_{10}/HT 3 and Cu_{10}-Nb_x/HT 3 are summarized in Table 1. The SSA of the Cu_{10}/HT 3 catalyst was 126 m^2/g. The addition of Nb to the catalyst caused a decrease in the SSA (from 123 to 90 m^2/g, respectively) and in the average pore diameter. With increasing Nb loading, this effect becomes more pronounced.

Table 2 reports the results of the TPD analyses as moles of NH_3 or CO_2 per weight unit. A combination of NH_3–TPD (ammonia temperature-programmed desorption) and CO_2–TPD (carbon dioxide temperature-programmed desorption) was used to quantify the density of acid and base sites on the catalysts.

The NH_3–TPD desorption profiles (Fig. 3, **left**) showed a broad peak at ≈180 °C assigned to the weak acid sites of the catalysts. The acid site density (total amount of μmol NH_3/g_{cat}) increases with increasing niobium loading, from 141 to 195 μmol NH_3/g_{cat}, confirming the acidic nature of this metal. In addition, the Cu_{10}/HT 3 catalyst showed a total acidity of 132 μmol NH_3/g_{cat}, demonstrating that the incorporation of

Table 1
SSA and pore size information of Cu_{10}/HT 3 and Cu_{10}-Nb_x/HT 3 catalysts.

Catalyst	SSA (m^2/g)	Pore size diameter (nm)
Cu_{10}/HT 3	126	6.5
Cu_{10}-$Nb_{0.5}$/HT 3	123	5.5
Cu_{10}-$Nb_{2.5}$/HT 3	121	5.3
Cu_{10}-Nb_5/HT 3	90	5.1
Cu_{10}-Nb_5/HT 3 (spent)	73	5.7

Table 2
Acidity and basicity of Cu_{10}/HT 3 and Cu_{10}-Nb_x/HT 3 catalysts from NH_3 and CO_2 TPD measurements.

Catalyst	μmol NH_3/g_{cat}	μmol CO_2/g_{cat}	Acid/base ratio
Cu_{10}/HT 3	132.0	262.0	0.50
Cu_{10}-$Nb_{0.5}$/HT 3	141.6	238.0	0.59
Cu_{10}-$Nb_{2.5}$/HT 3	175.9	222.2	0.79
Cu_{10}-Nb_5/HT 3	195.0	204.3	0.95

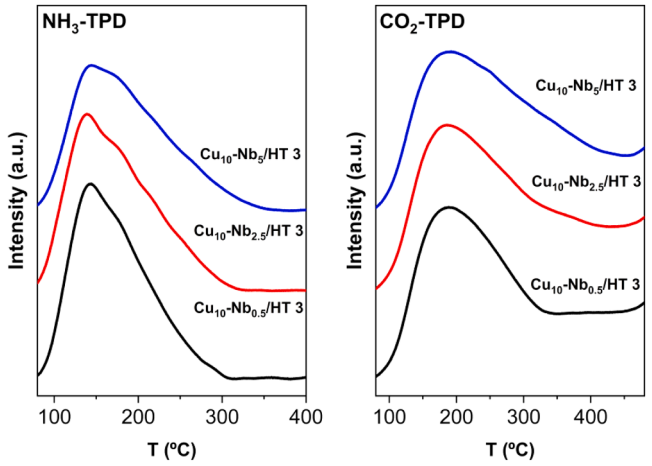

Fig. 3. NH_3– (left) and CO_2–TPD (right) profiles for the Cu_{10}-Nb_x/HT 3 catalysts – calcined at 400 ºC 2 h and in-situ reduced at 400 ºC with H_2 for 2 h.

niobium to the catalyst is responsible for the increase in its acidic properties. It has been reported that the acid sites promoted by the incorporation of Nb are of Brønsted and Lewis nature, mainly associated with the Nb═O bond of tetrahedral niobium [40].

The CO_2–TPD profiles of Cu_{10}-Nb_x/HT 3 catalysts (Fig. 3, **right**) indicated the presence of around 204–238 μmol CO_2/g_{cat} as the density of basic sites. The maximum peak was observed at ≈140 ºC. As shown in detail in Table 2, the basic site density of the Cu_{10}/HT 3 catalyst decreases from 262 to 204 μmol CO_2/g_{cat} with the gradual increase of Nb in the catalyst, demonstrating partial substitution of basic sites by acid sites of hydrotalcite. These data demonstrated how the distribution of acid and basic sites is modulated by the incorporation of Nb, with a higher Nb loading (Cu_{10}-Nb_5/HT 3 catalyst) promoting the presence of acid sites with a subsequent decrease in the number of basic sites. The acid/base ratio increased with Nb loading: 0.50, 0.59, 0.79 and 0.95, respectively.

The XPS technique was used to identify the oxidation state of the Cu species and determine the surface compositions of the catalysts and the possible effect of Nb incorporation into the catalyst by processing the spectra with the Multipak 9.6.0.15 package. Binding energy estimates were referenced to the C 1 s signal at 248.5 eV. The BEs were estimated with Gauss-Lorentz curves and a Shirley-type backdrop. The atomic concentration percentages of the distinctive elements were calculated using the corresponding area sensitivity factor for each detected spectral region. Table S1 summarizes all of the XPS measurements. The high-resolution Cu 2*p* core level spectrum of Cu_{10}-Nb_x/HT 3 (Fig. 4) showed two main peaks at around 952.6 eV and 932.6 eV, corresponding to the doublet Cu $2p_{1/2}$ - Cu $2p_{3/2}$, respectively [38,41,42]. The signal of Cu $2p_{3/2}$ of the Cu_{10}-$Nb_{2.5}$/HT 3 catalysts can be deconvoluted in two contributions. As was expected, Cu^{2+} was reduced to Cu^0 in agreement with XRD and H_2-TPR results. The Auger Cu_{LMM} signal (Fig. 5) is used to identify these oxidation states and determine the Cu value ($Cu^+ \approx 916.2$ eV; $Cu^0 \approx 918.2$ eV) [38,42]. Furthermore, from the XPS results of the reduced catalysts, partial surface reoxidation upon exposure to air occurs. Table 3 shows that the Cu^0/Cu^+ ratio gradually

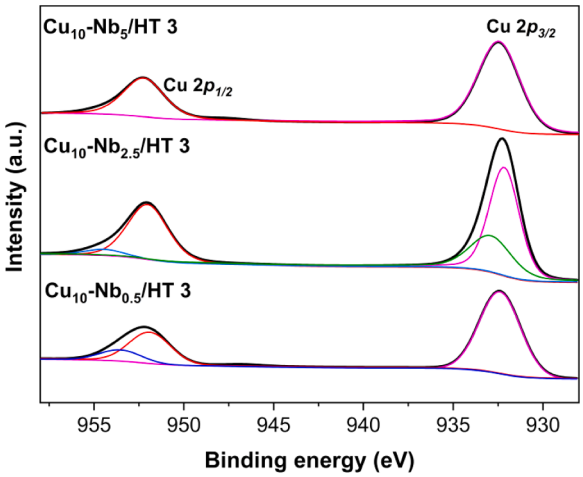

Fig. 4. XPS spectra of Cu $2p_{1/2}$ and Cu $2p_{3/2}$ region of Cu_{10}-Nb_x/HT 3 catalysts – calcined at 400 ºC for 2 h and ex-situ reduced at 400 ºC with H_2 for 2 h.

increased by the addition of Nb into the catalyst: 1.04, 1.06, 1.17 and 1.28, with Cu_{10}/HT 3, Cu_{10}-$Nb_{0.5}$/HT 3, Cu_{10}-$Nb_{2.5}$/HT 3 and Cu_{10}-Nb_5/HT 3, respectively. The Cu^0 and Cu^+ species coexist in our catalyst as expected [43]. Results showed that increasing the amount of Nb inhibited the partial oxidation of Cu^0 species, as the Cu^0/Cu^+ displayed.

Fig. 6 displays the high-resolution Nb 3*d* core level spectra and the binding energies values of the doublet Nb $3d_{5/2}$ Nb $3d_{3/2}$ of all Cu_{10}-Nb_x/HT 3 catalysts are indicated in Table 3. The Nb $3d_{5/2}$ (≈206.9 eV) and $3d_{3/2}$ (≈209.7 eV) peaks are assigned to the Nb_2O_5 species that calcination produced on the catalyst. No significant changes were observed in the shift of binding energies of the niobium signals, however, the intensity increased with Nb loading as expected.

Figure S3 shows the Mg 2*p*, Al 2 *s* and O 1 *s* of **a)** Cu_{10}-$Nb_{0.5}$/HT 3, **b)** Cu_{10}-$Nb_{2.5}$/HT 3 and **c)** Cu_{10}-Nb_5/HT 3, respectively. Mg 2*p* showed one peak at ≈49 eV attributable to the MgO species formed in the hydrotalcite materials after a thermal decomposition at high temperatures (500 ºC). The binding energy of Mg 2*p* shifted from 49.5 to 49.8 eV with increasing the Nb loading. The Al 2 *s* peaks have maxima at 118.7–118.8 eV and are assigned to Al(III). The O 1 s peak was deconvoluted in four contributions at ≈533 eV attributed to Nb═O [40], at ≈531 eV assigned to the oxygen from the CO_3^{2-} groups of the hydrotalcite structure and the carbonates adsorbed on the catalyst surface, the contribution at ≈530 eV was assigned to the oxygen bonds of OH^- on the hydrotalcite structure [44]. Finally, the contribution at ≈529 eV was attributed to O^{2-} [45].

The surface chemical composition of Cu_{10}/HT 3 and Cu_{10}-Nb_x/HT 3 catalysts obtained from XPS analysis are summarized in Table 3. The amount of Cu decreased from 4.6 to 3.2 wt% with the increase of Nb loading. This is attributed to the incorporation of Nb in the support and to the possible substitution of Cu. As anticipated, the amount of Nb increased with the increment of Nb in the impregnation. It should be spotted that the amount of Mg and Al decreased gradually as the Nb loading increased. This affected the molar ratio of Mg/Al, which dropped with the initial two loads (1.78 and 1.71), having a clearer effect with the 5% load, since the decrease in Al was higher, leading the Mg/Al ratio to climb up to 1.90.

3.2. Catalytic activity of Cu_{10}/HT 3 and Cu_{10}-Nb_x/HT 3 catalysts: influence of Nb content

The Guerbet condensation of ethanol was evaluated using 200 mg of catalyst at 180 ºC and 30 atm of nitrogen atmosphere in a batch reactor system and Fig. 7 shows the catalytic results**.** The ethanol conversion

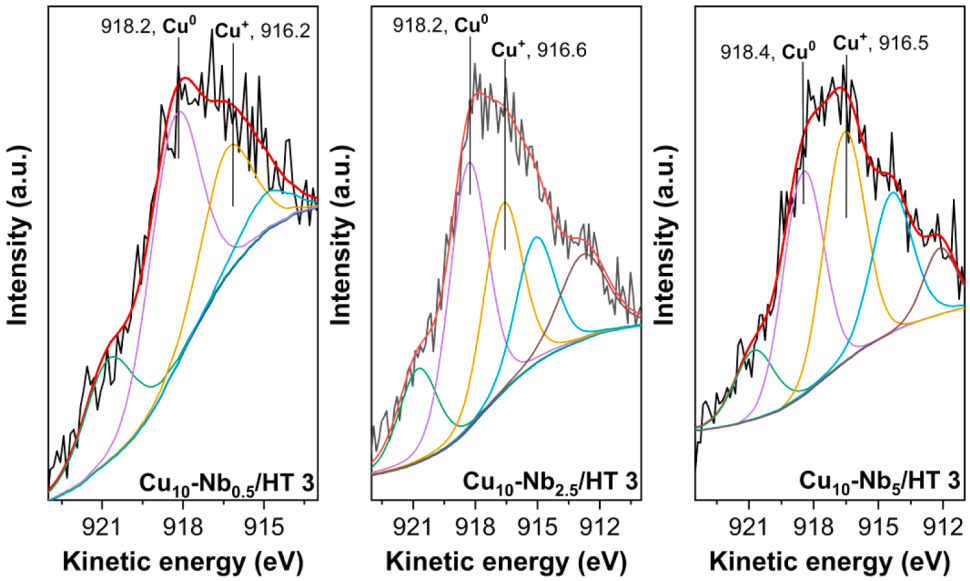

Fig. 5. Auger Cu_{LMM} spectra of Cu_{10}-Nb_x/HT 3 catalysts – calcined at 400 °C for 2 h and ex-situ reduced at 400 °C with H_2 for 2 h.

Table 3
Surface composition of Cu_{10}/HT 3 and Cu_{10}-Nb_x/HT 3 catalysts from XPS analysis.

Catalyst	wt% and (at%)						Surface Mg/Al molar ratio	Surface Cu^0/Cu^+ ratio
	Cu	Nb	Mg	Al	O	C		
Cu_{10}/HT 3	4.6 (1.4)	–	(21.6)	(10.2)	(47.5)	–	2.11	1.04
Cu_{10}-$Nb_{0.5}$/HT 3	3.6 (1.1)	4.1 (0.9)	(21.5)	(12.1)	(48.5)	–	1.78	1.06
Cu_{10}-$Nb_{2.5}$/HT 3	3.8 (1.3)	15.7 (3.7)	(19.2)	(11.2)	(48.6)	–	1.71	1.17
Cu_{10}-Nb_5/HT 3	3.2 (1.1)	21.5 (5.2)	(17.9)	(9.4)	(49.4)	(16.9)	1.90	1.28
Cu_{10}-Nb_5/HT 3 (spent)	2.8 (0.9)	10.6 (2.3)	(18.2)	(9.8)	(46.5)	(22.3)	1.86	0.79

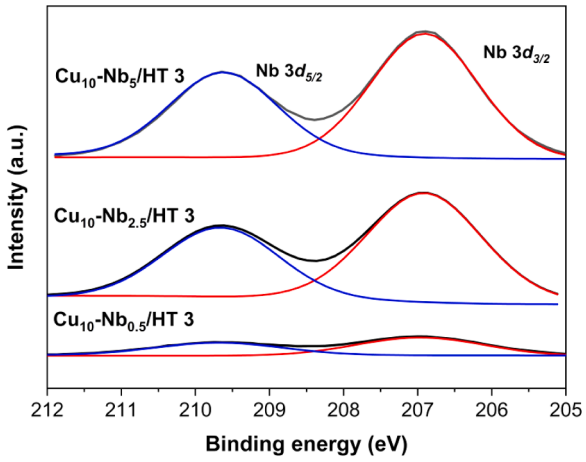

Fig. 6. XPS spectra of Nb $3d_{5/2}$ and Nb $3d_{3/2}$ region of Cu_{10}-Nb_x/HT 3 catalysts – calcined at 400 °C for 2 h and ex-situ reduced at 400 °C with H_2 for 2 h.

increases when the Nb loading is increased from Cu_{10}/HT 3 to Cu_{10}-Nb_5/HT 3. Subsequently, the conversion is related to the Nb content and the Cu^0/Cu^+ ratio (Table 3). Indeed, the catalyst with the highest Nb loading exhibited an ethanol conversion of 41% at 6 h and a selectivity of 94.4% towards *n*-BuOH. The main reaction products were *n*-butanol, 1-HexOH (4.2%) and Ace (1.4%). The catalyst without Nb showed the lowest EtOH conversion (18.3%), and selectivity towards *n*-BuOH (80.2%), with an increase in selectivity towards 1-HexOH (10.5%) and ACe (9.3%). These activity results can be related to low acid/base and Cu^0/Cu^+ ratios [46].

At 6 h, catalysts with the highest niobium concentration achieve an EtOH conversion of 42% with a selectivity to *n*-BuOH of 94.4% (yield to *n*-BuOH of 39.6%); in contrast, catalysts without Nb accomplish a conversion of 33.5% with a selectivity of 87.2% (yield to *n*-BuOH of 29.2%, Figure S4).

Although the selectivity achieved is remarkably comparable regardless of the catalysts used, the final carbon balance revealed that a considerable quantity of volatile compounds was not recovered in the reaction sample. These include acetic acid, ethyl acetate, crotonaldehyde, butanal, CO, and CO_2, etc. The carbon balances were between 42% and 62%, as the amount of Nb increased. Conducting the reaction in a continuous system allows us to overcome these drawbacks associated with the batch system. For this reason, it is proposed to carry out the reaction in a fixed–bed reactor, as discussed in the following section.

3.3. Catalytic condensation of ethanol in a fixed bed reactor: Influence of the temperature reaction

The Cu-Nb/HT 3 catalysts were tested in the ethanol condensation, at atmospheric pressure, in the gas phase at 150–350 °C, feeding to the catalytic bed with EtOH. The main products detected were *n*-BuOH, ACe, 1-HexOH, and AcOEt. Fig. 8 summarizes the results of the study of the temperature effect in the reaction.

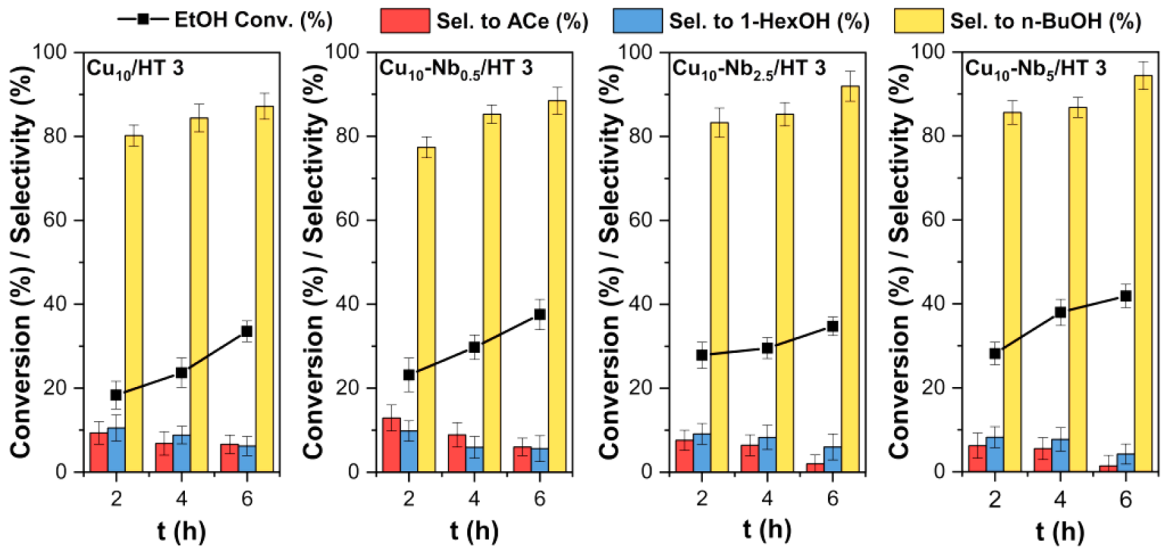

Fig. 7. Ethanol conversion and selectivities to ACe, 1-HexOH and n-BuOH in EtOH condensation over Cu_{10}/HT 3 and Cu_{10}-Nb_x/HT 3 in a batch reactor at 180 °C – samples pretreatment: calcined at 400 °C for 2 h and reduced at 400 °C with H_2 for 2 h (ex-situ).

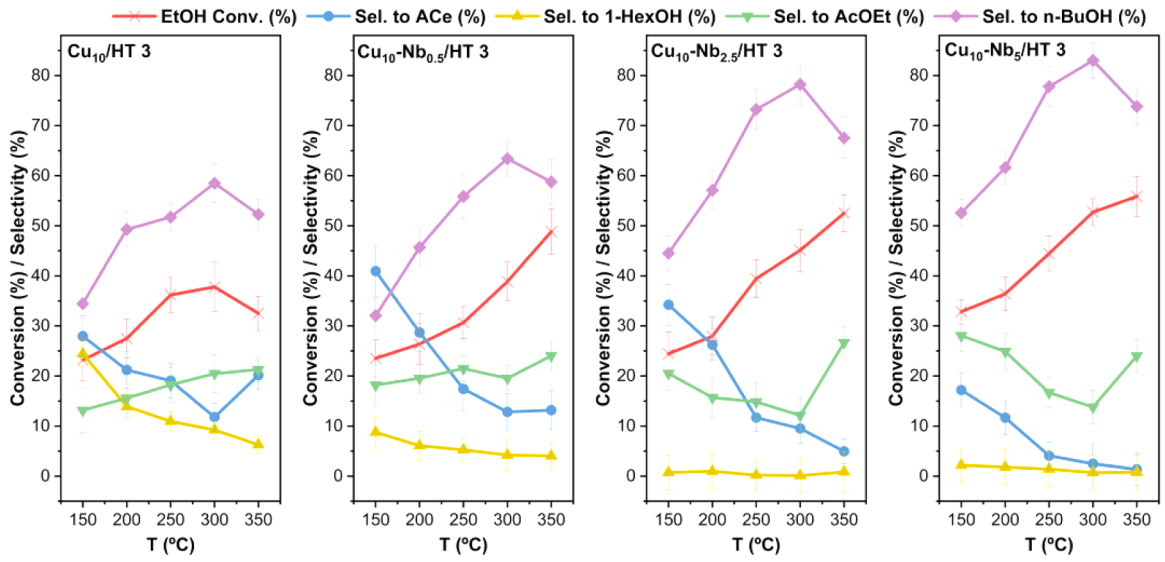

Fig. 8. Ethanol conversion and selectivity to Ace, 1-HexOH, AcOEt and n-BuOH for the EtOH and condensation over Cu_{10}/HT 3 and Cu_{10}-Nb_x/HT 3 catalyst in a fixed bed reactor. Reaction conditions: 150, 200, 250, 300 and 350 °C, 0.1 mL/min of EtOH, 200 mg of catalyst – samples pretreatment: calcined at 400 °C for 2 h and reduced at 400 °C with H_2 for 2 h (in-situ).

In the same manner as was observed when the reaction was carried out in the liquid phase, both the conversion of ethanol and the selectivity to *n*-BuOH increase with the Nb content. For catalysts with the highest Nb concentration, a conversion of 52.7% with a selectivity to *n*-BuOH of 83% (yield to *n*-BuOH of 43.8%, Figure S5) is achieved at 300 °C; whereas for the Nb-free catalyst, a conversion of 37.8% (Fig. 8) with a selectivity of 58.5% (yield to *n*-BuOH of 22.1%) is achieved.

The selectivity towards *n*-BuOH was higher at 300 °C and the yield increased with the Nb loading. This demonstrated the key role played by the acid sites provided by the Nb species during the condensation of acetaldehyde molecules to form *n*-BuOH by adsorbing the acetaldehyde molecules, whereas the basic sites remove the proton from this aldehyde as has been pointed out with other catalytic systems [14,46,47]. Nevertheless, it has been described that ethanol-derived adsorbates and hydride-like hydrogen are found on acidic sites primarily associated with the Nb species in the catalyst, whereas proton-like hydrogen is found on basic sites such as the MgO of hydrotalcite [35,48,49]. Furthermore, the coexistence of Cu^0/Cu^+ species promotes dehydrogenation/hydrogenation reactions [43]. Therefore, a good balance of these properties favors a higher selectivity towards *n*-BuOH, as revealed by the reaction results.

As mentioned above, acetaldehyde may be produced by the dehydrogenation of EtOH on basic sites and Cu species. The selectivity towards acetaldehyde decreased as the reaction temperature and ethanol conversion increased [23]; moreover, the selectivity decreased as the acid/base and Cu^0/Cu^+ ratios increased. In addition, 1-HexOH and AcOEt, were identified as the main byproducts in the absence of Nb in the catalyst formulation (Cu_{10}/HT 3). In the liquid phase (Fig. 7), higher selectivity for these compounds was also observed for Nb-free catalysts. Compared with the reaction in the batch system, the carbon balance in the continuous system ranges from 63% to 87%, demonstrating that the loss of volatile compounds is minimized in this reaction system.

3.4. Catalytic condensation of ethanol in a fixed bed reactor: time on stream study

The catalytic results for the Cu_{10}-Nb_5/HT 3 sample under time on stream (Figure S6 **a)** indicate that the performance is quite constant for at least 6 hours, whereas the selectivity towards *n*-BuOH remained stable until the fifth hour of the reaction, with values between 81−83%. However, selectivity decreased at the sixth hour, to 77%. The slight decrease in selectivity could be explained by catalyst deactivation resulting from coke generation. However, an increase in selectivity towards 1-HexOH was observed in addition to a decrease in selectivity towards AcOEt.

Therefore, a recycling study was carried out with the catalyst used in this reaction. Initially, the catalyst was recovered, dried, and studied employing nitrogen physisorption and XPS, this will be discussed below. The recycling study was performed for 6 h at 300 ºC with the same reaction conditions as the time on stream test. The recycling data (Figure S6 **b**) were compared with the performances obtained during the first cycle (Figure S6 **a**). The results showed that the EtOH conversion decreased slightly; nonetheless, there was a significant variation in selectivity towards *n*-BuOH, as it decreased barely and lacked the same stability over time as the fresh catalyst. This can be related to a decrease in the Cu^0/Cu^+ ratio or metal loss in the catalyst. Regardless of the decrease in EtOH conversion, the selectivity to ACe improved. Furthermore, the selectivity towards ethyl acetate decreased substantially. This could be due to the Nb species deactivation in the catalyst.

The surface composition of the spent catalyst was studied using XPS and the results are compared in Table 3. A slight decrease in the content of Cu on the spent catalyst was observed. Even yet, there was a slight variance in the surface Cu species, resulting in a large decrease in the Cu^0/Cu^+ ratio from 1.28 to 0.79 (Figure S7). This affects the selectivity towards the *n*-BuOH and EtOH conversion. Moreover, the molar ratio of Mg/Al slightly decreased from 1.90 to 1.86. The spent catalyst, on the other hand, showed a major change in the catalyst surface composition after the reaction, with the surface Nb decreasing by half. This could be a result of coke deposition on Nb particles. As a result of the process, the carbon content of the catalyst increased from 16.9 to 22.3 at%, indicating that coke had been deposited on its surface. In addition, NbO_2 was formed in the spent catalyst as a result of the reduction of Nb_2O_5 during the reaction (Figure S8).

The N_2 isotherms of the fresh and spent Cu_{10}-Nb_5/HT 3 catalyst are shown in Figure S9). A decrease from 90 to 73 m^2/g in SSA was shown in the spent Cu_{10}-Nb_5/HT 3 catalyst with respect to the fresh sample (Table 1). This could be attributed to a possible reconstruction of the hydrotalcite interlayer due to the water produced during the reaction, it is known as the "memory effect" [50]. Due to the decrease in SSA, the pore size increased from 5.1 to 5.7 nm.

4. Conclusions

It has been demonstrated that the addition of Nb to Cu-supported catalysts induces an increase in acid sites on the surface of the catalysts, along with an increment in the Cu^0/Cu^+ ratio associated with better catalytic performance during the synthesis of *n*-BuOH from ethanol, both in terms of selectivity, yield and conversion (94.4%, 39.6% and 42% in a batch system and 83%, 43.8% and 52.7% in a continuous system, respectively). In addition, the Cu-Nb-contained catalyst showed good stability under time on stream. Furthermore, a recycling study was carried out and the results displayed a moderate reduction of Nb surface species after the reaction, which affects *n*-BuOH selectivity.

CRediT authorship contribution statement

José J. Cano-Gómez: Resources, Methodology. **Isabel Barroso-Martín:** Methodology, Investigation. **Daniel A. Valdivieso-Vera:** Writing – review & editing, Writing – original draft, Methodology, Investigation, Formal analysis, Data curation. **Gerardo A. Flores-Escamilla:** Resources, Methodology. **M. Olga Guerrero-Perez:** Writing – review & editing, Writing – original draft, Supervision, Resources, Methodology, Investigation, Funding acquisition, Formal analysis, Conceptualization. **Enrique Rodríguez-Castellón:** Writing – review & editing, Methodology, Investigation, Funding acquisition, Data curation. **Iván A. Santos-López:** Writing – review & editing, Writing – original draft, Supervision, Methodology, Investigation, Funding acquisition, Data curation, Conceptualization.

Declaration of Competing Interest

The authors declare the following financial interests/personal relationships which may be considered as potential competing interests: Daniel Valdivieso reports financial support was provided by Consejo Nacional de Ciencia y Tecnología (CONACyT). Daniel Valdivieso reports financial support was provided by Asociación Universitaria Iberoamericana de Posgrado (AUIP). M. Olga Guerrero Perez reports financial support was provided by Spain Ministry of Science and Innovation. Ivan Santos-Lopez reports financial support was provided by PAICyT-UANL 2022. If there are other authors, they declare that they have no known competing financial interests or personal relationships that could have appeared to influence the work reported in this paper.

Data availability

No data was used for the research described in the article.

Acknowledgement

We acknowledge the financial support of this work by PAICyT-UANL 2022 (584-IT-2022). Financial support from project PID2021-126235OB-C32 funded by MCIN/ AEI/10.13039/501100011033/ and FEDER funds, and projects TED2021-130756B funded by MCIN/AEI/10.13039/501100011033 and by "ERDF A way of making Europe" by the European Union NextGenerationEU/PRTR is also acknowledged. Daniel Valdivieso acknowledges the Consejo Nacional de Ciencia y Tecnología (CONACyT) for PhD scholarship and the Asociación Universitaria Iberoamericana de Posgrado (AUIP) for the financial support granted. Funding for open access charge: Universidad de Málaga/CBUA.

Appendix A. Supporting information

Supplementary data associated with this article can be found in the online version at doi:10.1016/j.cattod.2024.114658.

References

[1] W.R. da S. Trindade, R.G. dos Santos, Review on the characteristics of butanol, its production and use as fuel in internal combustion engines, Renew. Sustain. Energy Rev. 69 (2017) 642–651, https://doi.org/10.1016/j.rser.2016.11.213.
[2] D.E. Ramey, Butanol: the other alternative fuel, Agric. Biofuels: Technol., Sustain. Profitab. 85 (2007) 137. ⟨https://www.researchgate.net/publication/284806414⟩.
[3] O.I. Shapovalov, L.A. Ashkinazi, Biobutanol: biofuel of second generation, Russ. J. Appl. Chem. 81 (2008) 2232–2236, https://doi.org/10.1134/S1070427208120379.
[4] M. Fenkl, M. Pechout, M. Vojtisek, N-butanol and isobutanol as alternatives to gasoline: Comparison of port fuel injector characteristics, EPJ Web Conf, EDP Sciences (2016), https://doi.org/10.1051/epjconf/201611402021.
[5] F.N. Alasfour, Butanol-A single cylinder engine study: engine performance, Int. J. Energy Res. 21 (1997) 21–30, https://doi.org/10.1016/S1359-4311(96)00069-5.
[6] J.H. Mack, D. Schuler, R.H. Butt, R.W. Dibble, Experimental investigation of butanol isomer combustion in Homogeneous Charge Compression Ignition (HCCI) engines, Appl. Energy 165 (2016) 612–626, https://doi.org/10.1016/j.apenergy.2015.12.105.
[7] T.C. Ezeji, H.P. Blaschek, Butanol production from lignocellulosic biomass, Biofuels Agric. Wastes Byprod. (2010) 19–37, https://doi.org/10.1002/9780813822716.ch3.

[8] H.A. Alalwan, A.H. Alminshid, H.A.S. Aljaafari, Promising evolution of biofuel generations. Subject review, Renew. Energy Focus 28 (2019) 127–139, https://doi.org/10.1016/j.ref.2018.12.006.
[9] N.S. Mat Aron, K.S. Khoo, K.W. Chew, P.L. Show, W.H. Chen, T.H.P. Nguyen, Sustainability of the four generations of biofuels – a review, Int. J. Energy Res. 44 (2020) 9266–9282, https://doi.org/10.1002/er.5557.
[10] K. Dutta, A. Daverey, J.G. Lin, Evolution retrospective for alternative fuels: first to fourth generation, Renew. Energy 69 (2014) 114–122, https://doi.org/10.1016/j.renene.2014.02.044.
[11] S. Veibel, J.I. Nielsen, On the mechanism of the Guerbet reaction, Tetrahedron 23 (1967) 1723–1733, https://doi.org/10.1016/S0040-4020(01)82571-0.
[12] J.T. Kozlowski, R.J. Davis, Heterogeneous catalysts for the guerbet coupling of alcohols, ACS Catal. 3 (2013) 1588–1600, https://doi.org/10.1021/cs400292f.
[13] T.W. Birky, J.T. Kozlowski, R.J. Davis, Isotopic transient analysis of the ethanol coupling reaction over magnesia, J. Catal. 298 (2013) 130–137, https://doi.org/10.1016/j.jcat.2012.11.014.
[14] S. Cimino, L. Lisi, S. Romanucci, Catalysts for conversion of ethanol to butanol: effect of acid-base and redox properties, Catal. Today 304 (2017) 58–63, https://doi.org/10.1016/j.cattod.2017.08.035.
[15] J. Shen, J.M. Kobe, Y. Chen, J.A. Dumesic, Synthesis and Surface Acid/Base Properties of Magnesium-Aluminum Mixed Oxides Obtained from Hydrotalcites, (n.d.). ⟨https://pubs.acs.org/sharingguidelines⟩.
[16] D.L. Carvalho, R.R. De Avillez, M.T. Rodrigues, L.E.P. Borges, L.G. Appel, Mg and Al mixed oxides and the synthesis of n-butanol from ethanol, Appl. Catal. A Gen. 415–416 (2012) 96–100, https://doi.org/10.1016/j.apcata.2011.12.009.
[17] P. Benito, A. Vaccari, C. Antonetti, D. Licursi, N. Schiarioli, E. Rodriguez-Castellón, A.M. Raspolli Galletti, Tunable copper-hydrotalcite derived mixed oxides for sustainable ethanol condensation to n-butanol in liquid phase, J. Clean. Prod. 209 (2019) 1614–1623, https://doi.org/10.1016/j.jclepro.2018.11.150.
[18] Z. Sun, A.C. Vasconcelos, G. Bottari, M.C.A. Stuart, G. Bonura, C. Cannilla, F. Frusteri, K. Barta, Efficient catalytic conversion of ethanol to 1-butanol via the guerbet reaction over copper- and nickel-doped porous, ACS Sustain Chem. Eng. 5 (2017) 1738–1746, https://doi.org/10.1021/acssuschemeng.6b02494.
[19] I.C. Marcu, N. Tanchoux, F. Fajula, D. Tichit, Catalytic conversion of ethanol into butanol over M-Mg-Al mixed oxide catalysts (M = Pd, Ag, Mn, Fe, Cu, Sm, Yb) obtained from LDH precursors, Catal. Lett. 143 (2013) 23–30, https://doi.org/10.1007/s10562-012-0935-9.
[20] G. Garbarino, P. Riani, M. Villa García, E. Finocchio, V. Sanchez Escribano, G. Busca, A study of ethanol dehydrogenation to acetaldehyde over copper/zinc aluminate catalysts, Catal. Today 354 (2020) 167–175, https://doi.org/10.1016/j.cattod.2019.01.002.
[21] X.N. Li, S.S. Peng, L.N. Feng, S.Q. Lu, L.J. Ma, M.B. Yue, One-pot synthesis of acidic and basic bifunctional catalysts to promote the conversion of ethanol to 1-butanol, Microporous Mesoporous Mater. 261 (2018) 44–50, https://doi.org/10.1016/j.micromeso.2017.11.004.
[22] T. Tsuchida, J. Kubo, T. Yoshioka, S. Sakuma, T. Takeguchi, W. Ueda, Reaction of ethanol over hydroxyapatite affected by Ca/P ratio of catalyst, J. Catal. 259 (2008) 183–189, https://doi.org/10.1016/j.jcat.2008.08.005.
[23] T. Tsuchida, S. Sakuma, T. Takeguchi, W. Ueda, Direct synthesis of n -butanol from ethanol over nonstoichiometric hydroxyapatite, Ind. Eng. Chem. Res 45 (2006) 8634–8642, https://doi.org/10.1021/ie0606082.
[24] S. Hanspal, Z.D. Young, J.T. Prillaman, R.J. Davis, Influence of surface acid and base sites on the Guerbet coupling of ethanol to butanol over metal phosphate catalysts, J. Catal. 352 (2017) 182–190, https://doi.org/10.1016/j.jcat.2017.04.036.
[25] L.C. Kao, W.C. Kan, R.M. Martin-Aranda, M.O. Guerrero-Perez, M. Bañares, S.Y. H. Liou, SiO2 supported niobium oxides with active acid sites for the catalytic acetalization of glycerol, Catal. Today 356 (2020) 80–87, https://doi.org/10.1016/j.cattod.2019.08.007.
[26] M.O. Guerrero-Pérez, J.L.G. Fierro, M.A. Bañares, Tunning the Nb addition to Sb-V-O catalysts for an efficient promotion of the ammoxidation of propane to acrylonitrile, Catal. Today 118 (2006) 366–372, https://doi.org/10.1016/j.cattod.2006.07.011.
[27] R. López-Medina, J.L.G. Fierro, M.O. Guerrero-Pérez, M.A. Bañares, Nanoscaled rutile active phase in Mo-V-Nb-O supported catalysts for the oxidation of propane to acrylic acid, Appl. Catal. A Gen. 375 (2010) 55–62, https://doi.org/10.1016/j.apcata.2009.12.017.
[28] X. Li, E. Iglesia, Selective catalytic oxidation of ethanol to acetic acid on dispersed Mo-V-Nb mixed oxides, Chem. - A Eur. J. 13 (2007) 9324–9330, https://doi.org/10.1002/chem.200700579.
[29] P. Jackson, K.J. Fisher, G.D. Willett, The catalytic activation of primary alcohols on niobium oxide surfaces unraveled: the gas phase reactions of NbxOy clusters with methanol and ethanol, Chem. Phys. 262 (2000) 179–187, https://doi.org/10.1016/S0301-0104(00)00304-9.
[30] E. Rojas, J.J. Delgado, M.O. Guerrero-Pérez, M.A. Bañares, Performance of NiO and Ni-Nb-O active phases during the ethane ammoxidation into acetonitrile, Catal. Sci. Technol. 3 (2013) 3173–3182, https://doi.org/10.1039/c3cy00415e.
[31] F. Rubio-Marcos, E. Rojas, R. López-Medina, M.O. Guerrero-Pérez, M.A. Bañares, J. F. Fernandez, Tuning of active sites in Ni-Nb-O catalysts for the direct conversion of ethane to acetonitrile or ethylene, ChemCatChem 3 (2011) 1637–1645, https://doi.org/10.1002/cctc.201100115.
[32] M.O. Guerrero-Pérez, M.A. Bañares, Niobium as promoting agent for selective oxidation reactions, Catal. Today 142 (2009) 245–251, https://doi.org/10.1016/j.cattod.2008.10.041.
[33] M.O. Guerrero-Pérez, The fascinating effect of niobium as catalytic promoting agent, Catal. Today 354 (2020) 19–25, https://doi.org/10.1016/j.cattod.2019.04.008.
[34] D. Stošić, F. Hosoglu, S. Bennici, A. Travert, M. Capron, F. Dumeignil, J. L. Couturier, J.L. Dubois, A. Auroux, Methanol and ethanol reactivity in the presence of hydrotalcites with Mg/Al ratios varying from 2 to 7, Catal. Commun. 89 (2017) 14–18, https://doi.org/10.1016/j.catcom.2016.10.013.
[35] K.K. Ramasamy, M. Gray, H. Job, D. Santosa, X.S. Li, A. Devaraj, A. Karkamkar, Y. Wang, Role of calcination temperature on the hydrotalcite derived MgO-Al2O3 in converting ethanol to butanol, Top. Catal. 59 (2016) 46–54, https://doi.org/10.1007/s11244-015-0504-8.
[36] G.F. Leal, S. Lima, I. Graça, H. Carrer, D.H. Barrett, E. Teixeira-Neto, A.A. S. Curvelo, C.B. Rodella, R. Rinaldi, Design of nickel supported on water-tolerant Nb2O5 catalysts for the hydrotreating of lignin streams obtained from lignin-first biorefining, IScience 15 (2019) 467–488, https://doi.org/10.1016/j.isci.2019.05.007.
[37] R.L. Kadam, Y. Kim, S. Gailkwad, M. Chang, N.H. Tarte, S. Han, Catalytic decolorization of rhodamine B, Congo red, and crystal violet dyes, with a novel niobium oxide anchored molybdenum (Nb–O–Mo), Catalysts 10 (2020), https://doi.org/10.3390/catal10050491.
[38] J. Guo, H. Yu, F. Dong, B. Zhu, W. Huang, S. Zhang, High efficiency and stability of Au-Cu/hydroxyapatite catalyst for the oxidation of carbon monoxide, RSC Adv. 7 (2017) 45420–45431, https://doi.org/10.1039/c7ra08781k.
[39] U. Iriarte-Velasco, J.L. Ayastuy, R. Bravo, Z. Boukha, M.A. Gutiérrez-Ortiz, Biogenic hydroxyapatite as novel catalytic support for Ni and Cu for the water–gas shift reaction, J. Mater. Sci. 56 (2021) 6745–6763, https://doi.org/10.1007/s10853-020-05724-x.
[40] C. García-Sancho, J.A. Cecilia, A. Moreno-Ruiz, J.M. Mérida-Robles, J. Santamaría-González, R. Moreno-Tost, P. Maireles-Torres, Influence of the niobium supported species on the catalytic dehydration of glycerol to acrolein, Appl. Catal. B 179 (2015) 139–149, https://doi.org/10.1016/j.apcatb.2015.05.014.
[41] W. Zhou, W. Lu, H. Wang, Z. Xia, S. Zhai, Z. Zhang, Y. Ma, M. He, Q. Chen, CuMgAl hydrotalcite as an efficient bifunctional catalyst for the cross-dehydrogenative C–C coupling reactions under mild conditions, Appl. Catal. A Gen. 604 (2020), https://doi.org/10.1016/j.apcata.2020.117771.
[42] M.C. Biesinger, Advanced analysis of copper X-ray photoelectron spectra, Surf. Interface Anal. 49 (2017) 1325–1334, https://doi.org/10.1002/sia.6239.
[43] H. Yang, Y. Chen, X. Cui, G. Wang, Y. Cen, T. Deng, W. Yan, J. Gao, S. Zhu, U. Olsbye, J. Wang, W. Fan, A highly stable copper-based catalyst for clarifying the catalytic roles of Cu0 and Cu+ species in methanol dehydrogenation, Angew. Chem. - Int. Ed. 57 (2018) 1836–1840, https://doi.org/10.1002/anie.201710605.
[44] G.C. Gomes, F.F. Borghi, R.O. Ospina, E.O. López, F.O. Borges, A. Mello, Nd:YAG (532 nm) pulsed laser deposition produces crystalline hydroxyapatite thin coatings at room temperature, Surf. Coat. Technol. 329 (2017) 174–183, https://doi.org/10.1016/j.surfcoat.2017.09.008.
[45] J. Chen, Y. Song, D. Shan, E.H. Han, Study of the in situ growth mechanism of Mg-Al hydrotalcite conversion film on AZ31 magnesium alloy, Corros. Sci. 63 (2012) 148–158, https://doi.org/10.1016/j.corsci.2012.05.022.
[46] S. Ogo, A. Onda, Y. Iwasa, K. Hara, A. Fukuoka, K. Yanagisawa, 1-Butanol synthesis from ethanol over strontium phosphate hydroxyapatite catalysts with various Sr/P ratios, J. Catal. 296 (2012) 24–30, https://doi.org/10.1016/j.jcat.2012.08.019.
[47] C.R. Ho, S. Shylesh, A.T. Bell, Mechanism and kinetics of ethanol coupling to butanol over hydroxyapatite, ACS Catal. 6 (2016) 939–948, https://doi.org/10.1021/acscatal.5b02672.
[48] Y. Xiang, R. Barbosa, X. Li, N. Kruse, Ternary cobalt-copper-niobium catalysts for the selective CO hydrogenation to higher alcohols, ACS Catal. 5 (2015) 2929–2934, https://doi.org/10.1021/acscatal.5b00388.
[49] M. Ziolek, I. Sobczak, The role of niobium component in heterogeneous catalysts, Catal. Today 285 (2017) 211–225, https://doi.org/10.1016/j.cattod.2016.12.013.
[50] J. Pérez-Ramírez, S. Abelló, N.M. Van Der Pers, Memory effect of activated Mg-Al hydrotalcite: In situ XRD studies during decomposition and gas-phase reconstruction, Chem. - A Eur. J. 13 (2007) 870–878, https://doi.org/10.1002/chem.200600767.